

Co-sputtering of A Thin Film Broadband Absorber Based on Self-Organized Plasmonic Cu Nanoparticles

Jonas Drewes, Nanda Perdana, Kevin Rogall, Torge Hartig, Marie Elis, Ulrich Schürmann, Felix Pohl, Moheb Abdelaziz, Thomas Strunskus, Lorenz Kienle, Mady Elbahri, Franz Faupel, Carsten Rockstuhl, and Alexander Vahl*


The efficient conversion of solar energy to heat is a prime challenge for solar thermal absorbers, and various material classes and device concepts are discussed. One exciting class of solar thermal absorbers are plasmonic broadband absorbers that rely on light absorption thanks to plasmonic resonances sustained in metallic nanoparticles. This work focuses on Cu/Al₂O₃ plasmonic absorbers, which consist of a thin film stack of a metallic Cu-mirror, a dielectric Al₂O₃ spacer, and an Al₂O₃/Cu-nanoparticle nanocomposite. This work explores two preparation routes for the Al₂O₃/Cu-nanoparticle nanocomposite, which rely on the self-organization of Cu nanoparticles from sputtered atoms, either in the gas phase (i.e., via gas aggregation source) or on the thin film surface (i.e., via simultaneous co-sputtering). While in either case, Cu-Al₂O₃-Al₂O₃/Cu absorbers with a low reflectivity over a broad wavelength regime are obtained, the simultaneous co-sputtering approach enabled better control over the film roughness and showed excellent agreement with dedicated simulations of the optical properties of the plasmonic absorber using a multi-scale modeling approach. Upon variation of the thickness and filling factor of the Al₂O₃/Cu nanocomposite layer, the optical properties of the plasmonic absorbers are tailored, reaching an integrated reflectance down to 0.17 (from 250 to 1600 nm).

1. Introduction

Renewable energy sources and their efficient utilization play a crucial role in overcoming the ecological and societal implications associated with the extensive usage of limited fossil fuels. Among various renewable energy sources, such as wind, geothermal, and tidal energy, solar energy is particularly interesting, as solar irradiation reaches up to 5000 times the current global power consumption.^[1] Different approaches are pursued to harvest solar energy and convert it into electricity, for example, by photovoltaic cells or photothermal processes and subsequent conversion to electricity. In all solar-thermal approaches, the solar radiation is first converted into heat and afterward used to power, e.g., steam engines, to produce electricity. There are several concepts for concentrated solar power plants, e.g., solar power towers (SPT) or parabolic trough collectors (PTC). In the SPT, the sunlight is focused by sun-tracking reflectors onto a central receiver placed at the top of a fixed tower.

J. Drewes, K. Rogall, T. Hartig, F. Pohl, M. Abdelaziz, T. Strunskus, F. Faupel, A. Vahl
 Department for Materials Science–Chair for Multicomponent Materials
 Faculty of Engineering
 Kiel University
 Kaiserstraße 2, D-24143 Kiel, Germany
 E-mail: alva@tf.uni-kiel.de
 N. Perdana, C. Rockstuhl
 Institute of Theoretical Solid-State Physics
 Karlsruhe Institute of Technology (KIT)
 76137 Karlsruhe, Germany

M. Elis, U. Schürmann, L. Kienle
 Department for Materials Science–Synthesis and Real Structure
 Faculty of Engineering
 Kiel University
 Kaiserstraße 2, D-24143 Kiel, Germany
 U. Schürmann, T. Strunskus, L. Kienle, F. Faupel, A. Vahl
 Kiel Nano
 Surface and Interface Science KiNSIS
 Kiel University
 Christian-Albrechts-Platz 4, D-24118 Kiel, Germany
 M. Elbahri
 Nanochemistry and Nanoengineering
 School of Chemical Engineering
 Department of Chemistry and Materials Science
 Aalto University
 Aalto 00076, Finland
 C. Rockstuhl
 Institute of Nanotechnology
 Karlsruhe Institute of Technology (KIT)
 76021 Karlsruhe, Germany

 The ORCID identification number(s) for the author(s) of this article can be found under <https://doi.org/10.1002/ppsc.202300102>

© 2023 The Authors. Particle & Particle Systems Characterization published by Wiley-VCH GmbH. This is an open access article under the terms of the Creative Commons Attribution-NonCommercial License, which permits use, distribution and reproduction in any medium, provided the original work is properly cited and is not used for commercial purposes.

DOI: 10.1002/ppsc.202300102

In the PTC, the sunlight is focused by parabolic reflectors onto an absorber tube where the heat is transferred to a fluid.^[2] Common to both approaches is the application of an absorber as an essential building block, which absorbs the sunlight over a broad range of the solar spectrum and converts incoming photons to heat. This absorber has to simultaneously meet demanding requirements, i.e., a high solar absorptance throughout the whole solar spectrum combined with a low thermal emittance as well as a sufficient thermal stability at the respective operating temperatures.^[3] For example, a commercial absorber coating used in SPTs absorbs 0.96 of the solar spectrum at near-normal incidence angles.^[4] Furthermore, the absorber material has to withstand elevated temperatures without degradation, be resistant to oxidation, and be hard to prevent damage in harsh environments.^[5] A broad range of absorber concepts has been developed, e.g., intrinsic absorbers,^[6,7] semiconductor coatings,^[8,9] multilayer coatings,^[10,11] textured surfaces,^[12,13] dielectric-metal-dielectric absorbers,^[14,15] and metal-dielectric composite coatings, also called cermet based absorbers.^[16,17]

Metal-dielectric composite coatings employ plasmonic nanoparticles (NPs), which show, in general, strong absorption from ultra-violet (UV) to near-infrared (NIR) wavelengths.^[18,19] The absorber consists of multiple layers, i.e., a metallic ground plate, a dielectric spacer, and a nanocomposite layer containing NPs in a dielectric matrix. In these structures, perfect absorption can be achieved because of the destructive interference of reflected light at the air to absorber interface and the light reflected multiple times in the cavity of the multilayer systems.^[20] When reflection is suppressed, the light is entirely absorbed because the metal ground plate prevents transmission. The absorption is in spectral ranges where the NPs sustain plasmonic resonances. These plasmonic resonances enhance the light-matter interaction and facilitate a compact geometry. While an individual spherical NP supports a plasmon polariton only at a well-defined wavelength, there are several options to broaden the absorption in the nanocomposite layer. This broadening can be achieved by tuning the filling factor (FF) (and hence the particle-particle distance) or the size distribution of NPs.

The materials considered in metal-dielectric composite absorbers are, e.g., Cu and Au in a SiO₂ matrix or W,^[18,21,22] TiN,^[23] Ag,^[24] and Cu in an Al₂O₃ matrix.^[3,19,25] In order to enhance the thermal stability of metal-dielectric composite coatings, additional metal, metal oxide or metal nitride thin films have been investigated as diffusion barriers.^[26] Considering the abundance and availability of its components, in particular, metal-dielectric composite absorbers based on inexpensive materials such as Cu-NPs and SiO₂ or Al₂O₃ matrices are promising. Recently, an Au-Al₂O₃-Al₂O₃/Cu-NP plasmonic absorber based on a combination of Al₂O₃/Cu-NP nanocomposite layer, Al₂O₃ spacer, and Au metallic ground plate was reported, which showed a low reflectivity over a broad spectral range.^[19] Multi-scale modeling indicated the potential of reaching up to 0.05 integrated reflectance in the wavelength regime from 250–1800 nm. The Al₂O₃/Cu-NP nanocomposite layer was obtained by embedding Cu-NPs, derived from gas phase synthesis, into a dielectric Al₂O₃ matrix. While this experimental approach offers excellent control over the FF and a well-defined and FF-independent NP size and size distribution, the obtained Au-Al₂O₃-Al₂O₃/Cu-NP plasmonic absorbers fell short of fully reaching the modeled reflectance values.

In this work, the concept of plasmonic Al₂O₃/Cu-NP nanocomposites is transferred to Cu-Al₂O₃-Al₂O₃/Cu absorber thin film stacks, which make use of a Cu metal ground plate and hence rely entirely on a selection of inexpensive, abundant materials such as Cu and Al₂O₃. Two vacuum-based strategies are employed and compared to prepare the Al₂O₃/Cu-NP nanocomposite. The formation of Cu-NP relies in both cases on the self-organization from sputtered atoms, on the one hand in the gas phase via gas aggregation source (GAS) and on the other hand on the thin film surface via simultaneous co-sputtering from two distinct sources for Cu and Al₂O₃. To investigate the impact of the choice of preparation method on morphological features of the nanocomposite layer, the size and shape of Cu-NPs, as well as their dependency on the FF are determined by scanning and transmission electron microscopy micrographs, and the surface roughness of absorber stacks is studied by atomic force microscopy. The optical properties of the resulting Cu-Al₂O₃-Al₂O₃/Cu absorbers are characterized by spectroscopic ellipsometry. Furthermore, a multi-scale modeling approach is applied to compute the optical response of Cu-Al₂O₃-Al₂O₃/Cu absorber thin film stacks while explicitly considering the experimentally determined size distribution of the Cu-NPs. In the co-sputtering approach, Cu-NP size and size distribution are closely linked to the FF of Cu-NPs in the nanocomposite, and these parameters crucially impact the optical response of the absorber. Thus, to explore the range of obtainable absorption properties using the co-sputtering approach and discover the boundaries of the predictive power of the chosen modeling approach, a systematic analysis of co-sputtered absorbers with variations in nanocomposite filling factor and thickness is presented. Lastly, dual-stack nanocomposite structures, which feature two layers of Al₂O₃/Cu nanocomposites, are examined and discussed as a feasible approach to introduce impedance matching and tailored size distributions to the absorber stack.

2. Results and Discussion

To compare the surface roughness and morphology of thin-film broadband absorbers produced by co-sputtering and the GAS, atomic force microscopy (AFM), and scanning electron microscopy (SEM) investigations were performed on samples with comparable FF. The results are shown in **Figure 1**. The sample produced by the GAS shows a root-mean-square (RMS) roughness of 10.6 nm and a difference between the minimum and maximum height of 39 nm, although the layer is only 110 nm thick. This roughness is so high that the determined thickness of the layer is potentially not entirely correct. The absorber prepared by co-sputtering is smoother and has an RMS roughness of 2.2 nm and a difference between the minimum and maximum height of 6.7 nm, roughly six times smaller than the GAS derived absorber. The SEM images of the GAS sample show that large structures are present with large and deep trenches between these structures. The co-sputtered absorber exhibits a more homogeneous appearance and smaller structures and trenches.

One particular characteristic of self-organized NPs via co-sputtering is the dependence of NP size on the FF in the nanocomposite. This is in contrast to NPs from the GAS, where the NP size is determined by the self-organization processes in the gas phase, and nanocomposites with a broad range of FFs can

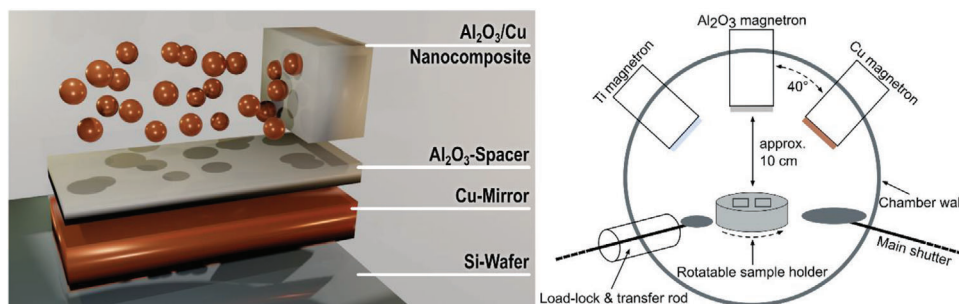


Figure 1. Left: Schematic of the cross-section of the plasmonic black absorber thin film stack. Right: Schematic drawing of the vacuum sputtering setup, consisting of separate magnetrons for the co-sputtering of Cu, Al₂O₃, and Ti.

be fabricated by embedding preformed NPs into the dielectric matrix. Transmission electron microscopy (TEM) investigations were performed to determine how the NP size distribution in co-sputtered absorbers develops for an increasing FF. Therefore, four samples with FF of 25%, 30%, 40%, and 50% were produced, and the resulting TEM micrographs and histograms of Cu-NP size distributions can be found in Figure S1 (Supporting Information). It is well visible that the NPs' mean diameter of the distribution increases for increasing FF. At an FF of 40%, the NPs are no longer well-separated islands, and deviations from spherical NPs are observed. Their density at 50 % is much higher in comparison to 40%. For higher FF such as 50%, the Cu-NP are no longer readily described by a circular outline, which implies significant deviations from a spherical shape of the Cu-NPs at higher FF. Therefore, diameter or radius are no longer meaningful quantities to describe the size of the Cu-NPs in the nanocomposite. In consequence, the area (i.e., the 2D projection of the NP to the viewing plane) of the NPs was determined and evaluated for the size distributions for each FF. The mean area of co-sputtered NPs is between ≈ 3 and ≈ 8 nm², which in turn is much lower than the mean area of the NPs produced by the GAS, which was ≈ 130 nm² (cf. Figure S2, Supporting Information). To determine the surface morphology of the Al₂O₃/Cu-NP nanocomposites at different FF, AFM, and SEM measurements were performed on co-sputtered nanocomposites with 25%, 32%, 40%, and 50% FF. The results are presented in Figure S3 (Supporting Information). From a comparison of the AFM maps and SEM micrographs, it can be concluded that the roughness increases for an increasing FF of the co-sputtered absorbers. In addition, the nanocomposite layers become less homogeneous for higher FF. However, compared to the absorbers produced via gas aggregation synthesis, the co-sputtered absorbers are more homogeneous and much smoother for all investigated FF.

In the following section, the optical properties of the smoother films produced via co-sputtering will be compared to the samples produced via GAS. Furthermore, the correlation between the simulated and experimentally obtained absorption curves will be compared for both synthesis approaches.

Figure 2 shows the measured (a) and simulated (b) reflectance spectra for two absorbers of comparable FF and nanocomposite thickness, one prepared by the co-sputtering method (32% FF and 100 nm nanocomposite thickness, blue line) and the other prepared using the GAS (33% FF and 104 nm nanocomposite thickness, red line). In a direct comparison of the experimentally obtained reflectance spectra for both absorbers (Figure 2a), the

absorber based on GAS exhibits slightly lower reflectance in the UV–vis regime (in particular ≈ 300 nm). In comparison, the co-sputtered absorber shows a lower reflectance in the near-infrared regime (in particular, ≈ 1300 nm). This observation may be attributed to the larger inter-particle distances of the GAS-derived Cu NPs since they are, on average, larger than the co-sputtered NPs, while the FFs are almost identical. Additionally, in contrast to Cu-NPs obtained via GAS, the shape of the Cu-NPs in the co-sputtered nanocomposite significantly deviates from a spherical shape. The shape affects the plasmonic response of the NPs, which can enhance or reduce the absorption of light, depending on the orientation of the NPs. A larger distance between the NPs reduces the red-shift of the plasmonic coupling, while a shorter distance red-shifts the plasmonic resonance frequency.^[27] This smaller inter-particle distance may cause the co-sputtered absorber to reflect less light than the absorber prepared by GAS in the range from ≈ 1100 to 1500 nm. Despite these relatively small differences, both absorbers generally show a comparable low reflectance over a broad wavelength range. This is also expressed in terms of the integrated reflectance in the range from 250 to 1600 nm, which will be considered as a figure of merit to compare the optical properties of different absorbers within this work. The integrated reflectance in the range is 0.207 for the co-sputtered absorber and 0.201 for the absorber prepared by the GAS.

The simulated reflectance spectra for both absorbers are compared in Figure 2b. In agreement with the experimentally obtained spectra, it is observed that the simulated GAS-derived absorber exhibits a lower reflectance than the co-sputtered one in the low wavelength range while exhibiting a larger reflectance in the longer wavelength regime. There is an excellent agreement between simulated and measured reflectance spectra for the co-sputtered absorbers (red lines in Figure 2a,b), both in terms of qualitative features (general shape of the curve and location of extrema) as well as in terms of quantitative reflectance values. While in the case of the GAS-derived absorbers, the simulated reflectance spectrum also covers the important qualitative features. For wavelengths longer than 1000 nm and above, the simulated reflectance spectrum shifts towards higher reflectance values than the experimentally obtained spectrum. The better agreement in the case of the co-sputtered absorber is likely due to the more homogeneous layer and the correspondingly lower surface roughness. Furthermore, it was also easier to determine the unit cell to model the co-sputtered absorber. Inhomogeneous thickness, high surface roughness, and touching particles of the

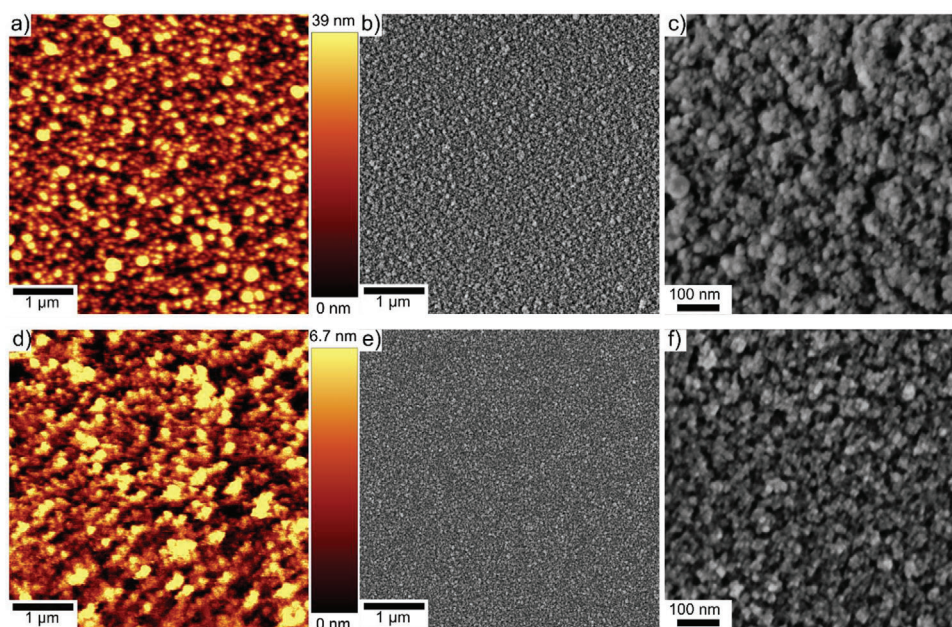


Figure 2. Comparison of AFM and SEM images of plasmonic black absorber thin films with a copper FF of 50% in the $\text{Al}_2\text{O}_3/\text{Cu}$ nanocomposite layer, fabricated via sequential GAS / RF co-sputtering a–c) and by simultaneous RF co-sputtering d–f). The co-sputtered sample shows a lower surface roughness compared to the GAS sample.

absorber from the GAS are considered the main reasons for the deviations of simulated and experimentally obtained reflectance spectra of the GAS-derived absorber.

In general, both experimentally prepared absorbers show a comparable overall reflectance. Considering the fabrication approach, the main drawback of applying a GAS traces back to its point-like deposition profile, which limits the attainable coating area and absorber size. In this context, using a co-sputtering approach to deposit the $\text{Al}_2\text{O}_3/\text{Cu}$ -NP nanocomposite not only yields a smoother film surface but also offers the benefit of potential upscaling, as co-sputtering is already applied to coat large surfaces, such as window glasses.^[28,29] Furthermore, in particular for the co-sputtered absorbers, the simulated and experimentally obtained reflectance curves are in excellent agreement. Thus, the multi-scale modeling provides a versatile platform to reproduce and predict the optical properties of plasmonic absorbers and can act as a guideline for designing co-sputtered $\text{Cu-Al}_2\text{O}_3\text{-Al}_2\text{O}_3/\text{Cu}$ thin film absorbers with tailored optical properties. In consequence, the following investigations in this work will focus on a detailed discussion of the optical properties of co-sputtered absorbers.

To determine the impact of the composition and thickness of the $\text{Al}_2\text{O}_3/\text{Cu}$ -NP nanocomposite on the optical properties of the plasmonic absorber, both parameters, FF (25%, 32 %, 40%, and 50%) and nanocomposite thickness (60, 80, 100, and 140 nm), have been varied systematically. In contrast, the other parameters, such as the thickness of the Al_2O_3 spacer layer and the metallic Cu mirror, were kept constant. The experimentally obtained and simulated reflectance spectra for each thin film stack are depicted in **Figure 3**.

Figure 3 shows the measured (left) and simulated (right) reflectance spectra for four different FFs at nanocomposite thicknesses of 60, 80, 100, and 140 nm. The comparison of experi-

mentally recorded reflectance spectra with changing FF shows that for 60, 80, and 100 nm thickness, there is an extension of the low reflectance regime toward longer wavelengths for increasing FF. Furthermore, at constant FF, the increase in total nanocomposite thickness also extends the low reflectance region towards longer wavelengths. However, such a shift in the low reflectance regime seems to be absent in thin film absorbers with 140 nm nanocomposite thickness, where for all FF, the reflectance is relatively low within the entire measurement range (i.e., from 245 to 1690 nm). Another interesting observation is that for higher nanocomposite layer thicknesses, an additional peak in the reflectance spectra appears: While for all investigated plasmonic absorbers the reflectance in the UV range up to 400 nm behaves quite similarly and lies below or ≈ 0.2 , with increasing nanocomposite layer thickness there is an increase in reflectance in the visible spectrum and near-infrared spectrum. This effect can be observed particularly for the 140 nm absorber stack, where the reflectance between 750 and 1200 nm approaches 0.4. Interestingly, in the case of the 140 nm nanocomposite layer thickness, an increase in FF reduces this additional peak, effectively straightening the reflectance spectrum and leading to a low reflectance below 0.30 throughout the investigated wavelength regime.

The reflectance spectra were also modeled for each combination of nanocomposite thickness and FF. **Figure 3** (right) compares the simulated reflectance spectra to the experimentally obtained spectra. In general, the simulated reflectance spectra are in good agreement with the experimentally obtained counterparts, and the general trends, as described in the context of the experimental data, are well reproduced also in the simulations. However, there is a notable deviation in the case of an FF of 50%. In the simulations, the plasmonic black absorbers with 50% FF in their nanocomposite layer systematically exhibit higher reflectance in

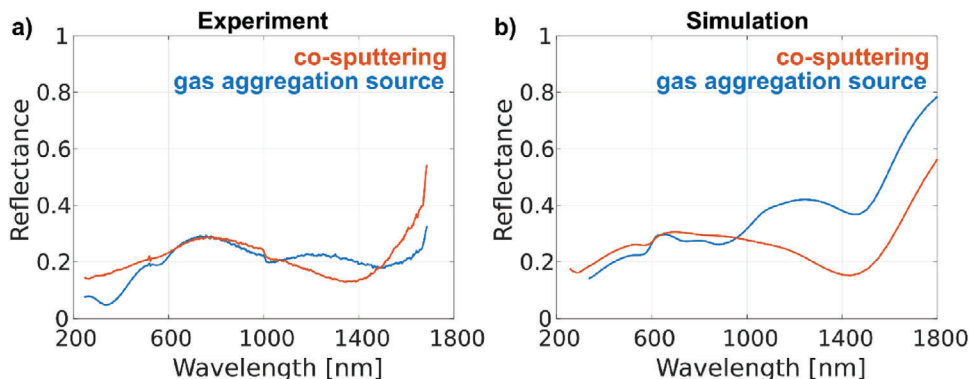


Figure 3. Optical properties for plasmonic thin film absorbers fabricated via GAS (104 nm nanocomposite thickness, 33% Cu FF, blue curves) and simultaneous co-sputtering (100 nm nanocomposite thickness, 32% Cu FF, red curves). The side-by-side comparison of the experimentally obtained a) and modeled b) reflectance spectra of both absorber stacks indicates a lower reflectance in the low wavelength regime in the case of GAS deposition, while the co-sputtered absorber exhibits lower reflectance in the near IR regime.

the simulated reflectance spectra. Here, three reasons can explain that discrepancy.

First, the model considers the NP size distribution determined experimentally and constructs a unit cell with perfectly spherical NPs as building units (cf. Figure S4, Supporting Information). While the assumption of spherical NPs is readily fulfilled with NPs from gas phase synthesis (such as GAS), the NP shape can significantly deviate from spherical shapes for co-sputtering and self-organization. Furthermore, for high FF, such as 50 %, the TEM investigations revealed the prevalence of irregular, non-spherical NPs (cf. Figure S1, Supporting Information).

Second, determining the NP size distribution (in terms of particle area) via bright field TEM requires thin nanocomposite layers with non-overlapping particles. This requirement is challenging and prone to errors for high FF because the target nanocomposite layer thickness in the absorber is far larger than in the reference TEM sample. Unlike NPs from gas phase synthesis, the NP size distribution in self-organized particles from co-sputtering is not independent of the FF and nanocomposite thickness.

Third, the current modeling approach does not consider the possibility that adjacent NPs could touch. However, in the experimentally obtained thin film absorbers, a fraction of NPs is expected to be in direct contact with each other, which is expected to increase for higher FF.

All in all, this highlights the validity limit of the currently applied modeling approach to low to intermediate FF and outlines potential pathways to increase the predictive power by considering surface roughness and non-spherical NPs in the multi-scale model. The former could be done by performing finite-difference time-domain (FDTD) simulations instead of using the thin-film transfer matrix technique. In the FDTD, a reasonably large supercell could be considered that captures these statistical details of the surface roughness. However, the spatial extent of these supercells would be quite large, which poses challenges to the available computational resources. The latter problem could be tackled by computing the T-matrix of such non-spherical or coalesced nanoparticles and considering these T-matrices instead of those available analytically for spheres. However,

this would require many more phenomenological assumptions concerning the statistical appearance of these non-spherical particles.

From the reflectance spectra, as shown in Figure 3, the integrated reflectance is calculated between 250 and 1600 nm, which serves as a measure for the overall relevant reflectance in solar absorber applications. In Figure 4, the heatmaps for the integrated reflectance are compared for the experimental and simulated absorbers of varying FF and nanocomposite thicknesses. The greyscale indicates the integrated reflectance, with 0.164 corresponding to the thin film absorber with the lowest reflectance (black, 80 nm nanocomposite with 50% FF) and 0.396 corresponding to the highest reflectance (white, 60 nm nanocomposite with 25% FF). For clarity, the numerical values for the integrated reflectance are collected in Table 1. Two major observations can be found in Figure 4: On the one hand, there is a significant deviation between the simulation and experiment for the absorber thin films with 50% FF, as discussed in detail in the previous section. On the other hand, both simulation and experiment show that the integrated reflectance cannot be reduced further by increasing the nanocomposite thickness above an optimum value. In all cases, the integrated reflectance of the 140 nm absorber is higher than that of the 100 nm counterpart.

So far, the plasmonic absorber thin film stacks, as investigated in this work, employed a single nanocomposite layer with a fixed FF of Cu-NPs in the dielectric Al_2O_3 matrix. As observed in Figure 4, at constant nanocomposite layer thickness, in these single-nanocomposite absorbers, a change in the FF results in a shift of the low-reflectance regime.

In the following, the focus will be shifted toward dual-nanocomposite absorbers. Here, the layout of the thin film stack is modified, as depicted in Figure 5 (right). The nanocomposite is divided into two separate layers with a different FF for each layer, resulting in a low- and high-FF layer. In Figure 5, two dual-nanocomposite absorbers with a total nanocomposite thickness of 80 nm (i.e., 40 nm high FF and 40 nm low FF) are compared, i.e., $\text{Cu-Al}_2\text{O}_3\text{-Al}_2\text{O}_3/\text{Cu}_{50\%}\text{FF-Al}_2\text{O}_3/\text{Cu}_{25\%}\text{FF}$ (50/25%, orange line) and $\text{Cu-Al}_2\text{O}_3\text{-Al}_2\text{O}_3/\text{Cu}_{25\%}\text{FF-Al}_2\text{O}_3/\text{Cu}_{50\%}\text{FF}$ (25/50%, blue line). Although both absorber stacks incorporate the same amount of Cu in the combined nanocomposite stacks, the

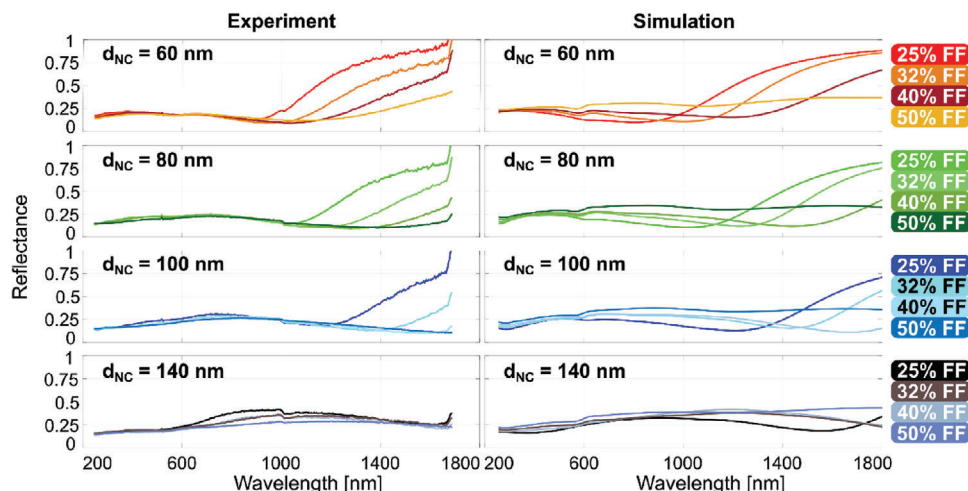


Figure 4. Measured (left) and simulated (right) impact of the nanocomposite layer on the optical properties of plasmonic thin-film absorbers prepared by simultaneous co-sputtering. The reflectance spectra (60° incidence) are compared for different nanocomposite film thicknesses (i.e., 60, 80, 100, and 140 nm, from top to bottom) and different FF (25%, 32%, 40%, and 50%).

Table 1. Comparison of integrated reflectance from 250 to 1600 nm (60° incidence) as obtained from spectroscopic ellipsometer measurements (red) and from multi-scale modeling (blue) for plasmonic absorbers with different nanocomposite film thickness and filling factor (cf. Figure 3)

Integrated Reflectance Experiment / Simulation		Filling factor							
		25%		32%		40%		50%	
Al ₂ O ₃ /Cu layer thickness	60 nm	0.396	0.312	0.288	0.251	0.220	0.210	0.183	0.293
	80 nm	0.326	0.236	0.223	0.213	0.179	0.215	0.164	0.301
	100 nm	0.294	0.207	0.207	0.240	0.199	0.257	0.200	0.327
	140 nm	0.299	0.255	0.260	0.321	0.275	0.313	0.239	0.348

stacking sequence 50/25% exhibits a lower integrated reflectance (0.167) compared to (0.189) the 25/50% sequence. From the reflectance spectra in Figure 5, it can be concluded that the 50/25% absorber has a lower reflectance than the 25/50% absorber from ≈250 to 1200 nm. One approach to explain the differences between both stacks can be found in the different effective mean refractive indices of the nanocomposite layers. With a refractive index closer to the surrounding medium (air) and having the 25%

FF nanocomposite layer to terminate the absorber stack will potentially lead to better impedance matching and a decrease in reflectance.

In contrast to the dual-nanocomposite absorbers, the single-nanocomposite absorbers with 25% or 50% FF exhibit an integrated reflectance of 0.326 and 0.164, respectively. The 25/50% absorber stack with its integrated reflectance of 0.189 lies between the single-nanocomposite absorbers with 32% and 40% FF (0.223 and 0.179, respectively). In contrast, the 50/25% dual-nanocomposite absorber exhibits an integrated reflectance of 0.167, which is considerably closer to the low integrated reflectance of the single-nanocomposite absorber with 50% FF (0.164). Consequently, the results from the dual-nanocomposite absorbers indicate that optimizing the reflectance spectra of plasmonic black absorbers is feasible.

The results on integrated reflectance for the Cu-Al₂O₃-Al₂O₃/Cu absorbers as investigated within this work (0.164) do not reach the low reflectance values of commercial absorbers (in c.f. absorbance of 0.96 at near normal incidences).^[4] However, in particular, under consideration of the low overall thickness of the absorber stack (20 nm Al₂O₃ spacer and 60–140 nm Al₂O₃/Cu-NP nanocomposite), the achieved optical properties show that

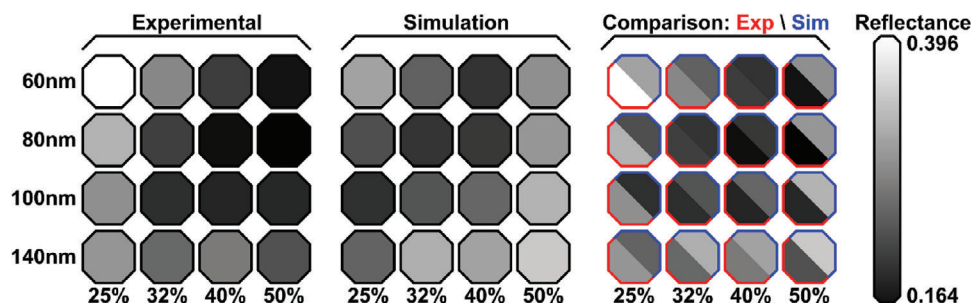


Figure 5. Heatmaps for the integrated reflectance from 250 to 1600 nm (60° incidence) for the experimentally recorded (left) and modeled reflectance spectra (middle). The nanocomposite film thicknesses, and FF correspond to those discussed in Figure 3. The greyscale represents the integrated reflectance, with white & black colors corresponding to the highest & lowest obtained reflectance, respectively. A direct comparison between the experiment and simulation is provided on the right panel.

the plasmonic Cu-Al₂O₃-Al₂O₃/Cu absorbers are promising for solar-thermal applications, e.g., on flexible substrates. However, direct comparison to similar absorbers and competing approaches are challenging because mainly the solar-weighted directional absorptance is determined, which covers a larger wavelength spectrum and also incorporates the solar intensity,^[24,30] which is beyond the scope of this work. Future studies on this class of plasmonic solar absorbers will need to address this measurement methodology and determine the absorbers' emissivity and thermal emittance at elevated temperatures.

Several pathways for further improvements of the optical properties of plasmonic absorbers open up. Based on the observations from the dual-nanocomposite absorbers, one promising path lies in a careful impedance matching to the surrounding medium, consequently tailoring the reflection of light at the first boundary. This could be approached by employing multiple nanocomposite layers with tailored FF or adding additional thin film coatings such as MgO or SiO₂. Furthermore, the comparison between GAS and co-sputtered absorbers has revealed the significant impact of Cu-NP shape, size, and distribution on the optical properties, indicating potential synergistic effects by incorporating varying Cu-NPs in the (multi)-nanocomposite.

3. Conclusion

In this work, plasmonic Cu-Al₂O₃-Al₂O₃/Cu-NP absorbers were studied, which employ a nanocomposite of Cu-NPs within an Al₂O₃ dielectric matrix to absorb light over a broad wavelength spectrum. In addition, two experimental approaches are explored to fabricate the Al₂O₃/Cu-NP nanocomposite layers: The Cu-NPs in the nanocomposite layer are either generated by gas phase synthesis in a GAS or via self-organization from Cu-atoms in a co-sputtering approach.

The choice of deposition technique strongly impacted the absorbers' morphology, topography, and optical properties. Co-sputtered absorbers exhibit a significantly lower surface roughness than GAS-derived absorbers, resulting in a more homogeneous absorber thin film stack. A main contribution to the difference in surface roughness and morphology traces back to the shape and size of Cu-NPs in the nanocomposite: While in the case of GAS-derived absorbers, preformed and comparably large Cu-NPs (mean area in the range of 100 nm²) with an approximately spherical shape are incorporated into the Al₂O₃ matrix, for co-sputtered absorbers the Cu-NPs are considerably smaller (mean area in the range of 5 nm²), deviate from a spherical shape and are formed directly on the surface of the nanocomposite thin film during growth. One crucial characteristic of Al₂O₃/Cu-NP nanocomposites obtained by co-sputtering is the intrinsic link between the nanocomposite's FF (i.e., the ratio between Cu-NPs and Al₂O₃ matrix) and the shape and size of the Cu-NPs within the nanocomposite.

The optical properties of a broad range of Cu-Al₂O₃-Al₂O₃/Cu-NP absorbers with varying FF and nanocomposite thickness were investigated by recording the reflectance spectra of the fabricated absorbers (at an incidence angle of 60°). The integrated reflectance in the wavelength range from 250 to 1600 nm was determined as a means to compare different absorber arrangements. The experimental studies are corroborated by simulated reflectance spectra obtained from a multi-scale modeling ap-

proach. In general, there is an excellent agreement between experimentally determined and simulated reflectance spectra for Cu-Al₂O₃-Al₂O₃/Cu-NP absorbers, which highlights the suitability of the chosen T-matrix multi-scale modeling approach for simulating the optical properties of these absorbers. However, there are two noteworthy exceptions where significant deviations between experimental and simulated reflectance spectra arise: On the one hand, for the GAS-derived absorber, where the high surface roughness and inhomogeneous morphology of the nanocomposites is not incorporated in the unit cell that is the basis of the chosen model. On the other hand, for co-sputtered absorbers at high FFs of 50%, where there is a substantial deviation from a spherical shape of the Cu-NPs, which, again, is not considered in the model.

With an integrated reflectance down to 0.164 (at 80 nm nanocomposite layer with 50% FF), it is demonstrated that co-sputtered Cu-Al₂O₃-Al₂O₃/Cu-NP absorbers are capable of showing a low reflectance over a broad wavelength regime. While the optical properties of the co-sputtered absorbers are generally comparable to GAS-derived absorbers, the co-sputtered absorbers offer the benefit of lower surface roughness and better homogeneity, as well as a better scaling potential towards a deposition on larger surface areas. However, prior to any scaling considerations, it is imperative to address challenges in terms of optical properties (i.e., further decreasing integrated reflectance and measuring under solar-like conditions). Potential pathways to improve the optical properties include incorporating multiple nanocomposite layers with tailored FF and size distributions and incorporating additional thin films to tailor the impedance matching between the absorber and the surrounding. Further improvements within this vast parameter space make it mandatory to supplement any experimental work with adequate modeling. The multi-scale modeling approach, with its capability to describe the optical properties of co-sputtered absorbers with an excellent agreement to the experimentally obtained reflectance spectra, has the potential to provide suitable predictive power to facilitate further studies on plasmonic metal-dielectric absorbers.

4. Experimental Section

Preparation of Thin Film Absorbers: In this work, Cu-Al₂O₃-Al₂O₃/Cu nanocomposite absorbers were fabricated via physical vapor deposition techniques (i.e., magnetron sputter deposition in direct current (DC) or radio frequency (RF) mode) in a custom-built high vacuum deposition system. The Cu-Al₂O₃-Al₂O₃/Cu nanocomposite absorbers comprise a multilayer thin film stack schematically depicted in **Figure 6** (left).

The Cu-Al₂O₃-Al₂O₃/Cu nanocomposite absorbers consist of the following:

Substrate: A plain Si wafer (p-doped Si wafer, with (100)-orientation and a native oxide layer, cut to 10 × 10 mm² pieces) was used as a substrate. The substrate was cleaned with isopropanol and dry nitrogen prior to the consecutive deposition steps.

Adhesion promoter: An adhesion promotion layer of titanium with a thickness of 10 nm was applied to the substrates by DC magnetron sputter deposition.

Metallic mirror / metallic ground plate: A 200 nm copper layer is the first layer that constitutes the actual absorber, of which an illustration is shown in the left of **Figure 6**. 200 nm was sufficient to be fully opaque. This layer corresponds to the metallic ground plate. This layer was deposited with an argon gas flow of 100 sccm at a pressure of 6.2 × 10⁻³ mbar (base pressure of 7 × 10⁻⁷ mbar) and a supplied DC power of 50 W.

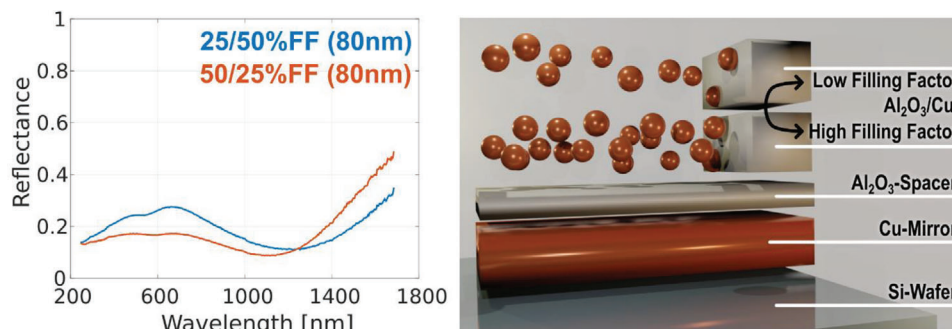


Figure 6. Reflectance spectra (60° incidence) for two dual-nanocomposite absorber thin film stacks, as recorded via spectroscopic ellipsometry (left). The dual-nanocomposite plasmonic black absorber thin films consist of two stacks of Al₂O₃/Cu nanocomposite thin films with an individual layer thickness of 40 nm and different FF (i.e., 25% and 50%). Two stacking sequences are compared here, namely Cu-Al₂O₃-Al₂O₃/Cu_{50%FF}-Al₂O₃/Cu_{25%FF} (50/25%, orange line) and Cu-Al₂O₃-Al₂O₃/Cu_{25%FF}-Al₂O₃/Cu_{50%FF} (25/50%, blue line).

Dielectric spacer layer: On top of the Cu thin film, the dielectric spacer layer of 20 nm Al₂O₃ was deposited at the same system pressure via RF magnetron sputter deposition at constant 60 W (60 W forward power and 1 W reflected power).

Nanocomposite layer: For the fabrication of the Al₂O₃/Cu-NP nanocomposite layer, two preparation routes based on self-organization of Cu-NPs from sputtered atoms either in the gas phase (i.e., via GAS) or on the thin film surface (i.e., via simultaneous co-sputtering) were explored.

The first approach employs a custom-made GAS, where a supersaturated vapor of Cu atoms was generated by sputtering from a 2-inch Cu target (99.99% purity) via DC magnetron sputtering (70 W). Via nucleation, growth, and coalescence, Cu-NPs were generated inside the source volume, which is separated from the main vacuum chamber by a circular orifice with 3 mm diameter. Thus, an NP beam of Cu-NPs was generated and projected toward the substrate surface. Then, in a consecutive co-deposition approach with a GAS and an RF-magnetron (forward power 84 W, reflected power 4 W) with a 2-inch Al₂O₃ target, Cu-NPs were embedded into an Al₂O₃ matrix. The deposition process of Al₂O₃/Cu-NP nanocomposite thin films and the underlying vacuum system are described in full detail in [19].

The second approach employs simultaneous co-sputtering from Al₂O₃ and Cu targets to generate Cu-NPs on the growth front via self-organization. Here, a custom-made magnetron sputtering vacuum chamber is applied, as depicted in Figure 6 (right). The vacuum chamber was evacuated using a turbomolecular pump (Pfeiffer HiPace 300) and a multistage roots dry pump (Pfeiffer ACP 28). Additionally, a load-lock was used for a more efficient sample introduction and extraction to and from the main chamber. This load-lock was evacuated by the same multistage root dry pump and an additional turbomolecular pump (Pfeiffer HiPace 80). The main chamber houses three water-cooled magnetrons (Planar-magnetron Ion'X-2UHV 9254), each with a two-inch magnetron target (Cu 99.99% purity, Al₂O₃ 99.99% purity, Ti 99.99% purity). The alumina (Al₂O₃) RF-magnetron was situated directly above the rotatable sample holder base onto that the samples are fixed. The sample holder base was rotated during the deposition using a step motor (PD 42-3-1140). The copper (Cu) and titanium (Ti) DC-magnetrons are positioned at an angle of 40° to the central magnetron. The argon gas was injected into the magnetrons using a gas flow controller (MKS 647C Gas Flow System) and was set to 100 sccm for all magnetrons. The two DC-magnetrons are each powered by a DC power supply (MDX500). The Al₂O₃ RF-magnetron was powered by an RF power supply (Cesar 600 WRF) and is operated at a constant 60 W (60 W forward power and 1 W reflected power) for all depositions. The DC power to the Cu magnetron was adjusted depending on the desired filling factor and nanocomposite thickness. The thickness of each layer was determined by previously establishing the deposition rate for each target. The Al₂O₃/Cu-NP nanocomposite layer was deposited by simultaneously depositing Al₂O₃ and Cu. The system pressure during this co-sputtering was also 6.2×10^{-3} mbar. The DC power to the Cu mag-

netron was set to 5, 7, 10, or 15 W to obtain filling factors of 25%, 32%, 40%, or 50%, respectively.

Characterization of Plasmonic Absorber Thin Films: The morphology of Cu-Al₂O₃-Al₂O₃/Cu thin film absorbers was studied via scanning electron microscopy (SEM) in a top-view configuration using the in-lens detector of a Gemini Ultra 55 plus microscope (Zeiss, Germany). To determine the FF of the Al₂O₃/Cu nanocomposite layer, the respective nanocomposite was deposited onto a substrate without a metallic Cu mirror and investigated via energy dispersive x-ray spectroscopy (EDX) using an Ultim Max 65 detector (Oxford Instruments, United Kingdom). Further details on the methodology to estimate the filling factor in the Al₂O₃/Cu nanocomposite layer from the experimentally obtained Cu/Al ratio are described elsewhere.[19]

An AFM (alpha300 RA -Raman-AFM- Microscope, WITec) was used to measure the surface topography using AC240 TS AFM tips (Asylum Research) in AC Mode. An area of 5 μm x 5 μm was probed by measuring 512 x 512 points. That leads to a spatial resolution below 10 nm. The Gwyddion data analysis software version 2.62 was used to determine the roughness.

Transmission electron microscopy (TEM) was used to image the co-sputtered nanocomposite for particle size measurements. For the TEM investigations, nanocomposite layers with a spacer thickness of 20 nm and a nanocomposite layer thickness of 20 nm were prepared directly on a TEM grid (Ni mesh 300 with C film, Plano EM, S160N3) to ensure transmission for the electron beam. Layers of Al₂O₃/Cu nanocomposite with filling factors of 25%, 32%, 40%, and 50% were deposited. Bright-field images were acquired using a Tecnai F30 G² (FEI) operating at 300 kV acceleration voltage.

To determine the optical properties of the Cu-Al₂O₃-Al₂O₃/Cu thin film absorbers, a spectroscopic ellipsometer (M2000-UI, J.A. Woollam) was used, and the reflectance of the thin film stacks was measured. The ellipsometer utilizes a 32 W deuterium lamp and a 20 W quartz tungsten halogen lamp, resulting in a total spectral range from 245 to 1690 nm. Additionally, a fixed polarizer is used to polarize the incident light linearly. The reflectance is measured at the center of each sample, at incidence angles from 45° to 75° in steps of 5°. The software CompleteEase (J.A. Woollam) was used to record the ellipsometer data and to control the device.

Light transmission can safely be neglected since the entire absorber, with its metallic mirror that acts as a ground plate, was optically thick. The total reflectance (*R*) at an incidence angle of 60° was calculated by integrating the reflectance curve in the relevant spectral domain and dividing it by the integral of the reflectance from a perfect reflector. This results in the following formula for the absorptance (*A*):

$$A = 1 - R = 1 - \frac{\int_{250 \text{ nm}}^{1600 \text{ nm}} R_{60^\circ}(\lambda) d\lambda}{\int_{250 \text{ nm}}^{1600 \text{ nm}} d\lambda} \quad (1)$$

Simulation: A multi-scale modeling approach to predict the reflectance from the samples on computational grounds was applied. The overarching idea was the following. First, the optical response from a cluster containing a larger number of metallic NPs and express it with a single T-Matrix was computed. That T-matrix was a crucial component of the scattering theory. Then, the reflection and transmission from a thin film consisting of a periodic arrangement of such clusters upon plane wave illumination was calculated and retrieve effective material parameters for the cluster material from the complex reflection and transmission coefficients. These effective material parameters capture the optical properties of the nanocomposite. Once we know these effective material parameters, we can consider them in an algorithm that calculates the optical response from homogenous stratified media. These quantities can then be compared to measured ones. The considered stratified media corresponds to the experimental layer stack. It was provided more details in the following.

Technically, it was started in this multi-scale modeling framework with the geometrical construction of the cluster. Here, multiple spherical NPs packed into a cubical volume was consider. The number of NPs and their diameters, as determined by the TEM measurements in the experimental procedures, were explicitly considered. The size of the cubical volume controls the FF of the nanocomposite. It was shown an example in Figure S4 (Supporting Information) for an FF = 40%. In the construction process, the NPs were closely packed randomly while it was imposed periodic boundaries at the edge of the cubical volume. The actual arrangement was made using the force-biased method for each FF.^[31] Considering periodic boundaries was important to prevent artifacts. It allows us to consider a geometrically infinite 2D layer in a following computational step, where the layer consists of a periodic arrangement of clusters of particles without any overlapping of particles in adjacent periods.

Next, the optical response from the cluster in a scattering theory that relies at its heart on Mie theory was calculated. In the Mie theory, the incident and scattered field from each scatterer at a certain frequency was expanded into vector spherical wave functions, $M_{mn}^{(j)}(r)$ and $N_{mn}^{(j)}(r)$, as:

$$E_{\text{inc}}(r) = \sum_{n=1}^{\infty} \sum_{m=-n}^n p_{mn} N_{mn}^{(1)}(r) + q_{mn} M_{mn}^{(1)}(r) \quad (2)$$

$$E_{\text{sca}}(r) = \sum_{n=1}^{\infty} \sum_{m=-n}^n a_{mn} N_{mn}^{(3)}(r) + b_{mn} M_{mn}^{(3)}(r) \quad (3)$$

where $J = \{1, 3\}$ is the pointer to the vector spherical wave function that relates to an incident or scattered fields. It translates to a specific type of spherical Bessel function term used in the definition of the vector spherical wave function.^[32] Ideally, the expansion is done from the first multipolar order ($n = 1$) to infinity. However, for all practical purposes, the sum can be truncated, and we consider up to the eighth multipolar order ($n = 8$) in the expansion of the optical response of the cluster. Then, the expansion coefficients, a_{mn} , b_{mn} , p_{mn} , q_{mn} , can be linked to a T-matrix T by the following relation.

$$\begin{pmatrix} a_{11} \\ \vdots \\ a_{mn} \\ b_{11} \\ \vdots \\ b_{mn} \end{pmatrix} = T \begin{pmatrix} p_{11} \\ \vdots \\ p_{mn} \\ q_{11} \\ \vdots \\ q_{mn} \end{pmatrix} \quad (4)$$

Using the T-matrix, we can find the physical properties of a scatterer, e.g., its extinction cross-section,^[33] and the material can also be homogenized.^[34] While the T-matrix was known for each NP and contains the Mie coefficients on its diagonal, for a cluster of particles, the collection of individual particle T-matrices corresponding to each particle center of coordinate can be expressed in one single coordinate system. This T-matrix was called the global T-matrix. The global T-matrix can be derived by transforming the local particle T-matrix with the addition theorem of the vector spherical wave function.^[35] The global T-matrix contains,

in linear approximation, all the optical properties of the individual cluster that was considered. It expresses how an incident field, expanded into vector spherical waves, is converted into a scattered field, equally expanded into vector spherical waves.

In further steps, a thin film consisting of periodically arranged clusters of particles along two dimensions was considered. The height of the film corresponds to the size of the considered unit cell. Next, it was considered that the layer was illuminated with a linearly polarized plane wave at a specific frequency at normal incidence, and we can compute the reflection and transmission coefficient from the layer using a periodic T-matrix scattering algorithm.^[35] Since the unpolarized wave is used as the incident wave in the step of characterization of the thin film, we can find the reflectance of an unpolarized wave illumination by using Equation 5. The reflectance of unpolarized wave (R_{unp}) is equal to the average reflectance of s-polarized (R_s) and p-polarized (R_p) waves as:

$$R_{\text{unp}} = \frac{R_s + R_p}{2} \quad (5)$$

However, until this point, the thickness of the NP layer was defined by the particle packing procedure described initially and cannot be varied freely. So, in the next stage, we find the effective optical permittivity of the layer to change the thickness in the following continuously.^[36] We do so by inverting the numerically computed reflection and transmission coefficients.

Finally, a multilayer system consisting of a layer containing the periodically arranged cluster of NPs, an alumina spacer layer, and a thick copper mirror is constructed. The thickness of the alumina spacer layer to 20 nm was fixed and vary the NP layer thickness. Please note that in all simulations it was considered an incidence angle of 60° in full agreement with the experimental scenario considered. The reflectance from the system at last was calculated using the transfer matrix method.^[37] This framework allows us to predict the optical properties that were also measured.

Supporting Information

Supporting Information is available from the Wiley Online Library or from the author.

Acknowledgements

This work had been funded by the Deutsche Forschungsgemeinschaft (DFG, German Research Foundation) – project number 413974664, i.e., projects RO 3640/12-1 and FA 234/32-1 as well as by DFG-Grant KI 1263/21-1.

Open access funding enabled and organized by Projekt DEAL.

Conflict of Interest

The authors declare no conflict of interest.

Author Contributions

C.R., F.F., T.S., and M.El.b. conceptualized the thin film stack plasmonic black absorber. A.V. and J.D. conducted SEM and EDX studies and evaluated, together with K.R. and F.P., the obtained results concerning morphology and filling factor. F.P., K.R., J.D., and M.A. deposited the Cu-Al₂O₃-Al₂O₃/Cu thin film absorbers via co-sputtering or gas aggregation and characterized the optical properties via spectroscopic ellipsometry. N.P. performed the simulations of the optical properties of the thin film absorbers. J.D., K.R., and A.V. wrote the initial draft of the manuscript. T.H. conducted AFM measurements and characterized the topography and

roughness of absorbers from gas aggregation source and co-sputtering. M.Eli. performed TEM investigations on the Al₂O₃/Cu nanocomposite thin films at different filling factors. F.F., T.S., and A.V. supervised the work of K.R., F.P., T.H., and J.D. L.K. and U.S. supervised the work of M.Eli. C.R. supervised the work of N.P. All authors discussed the results on the optical properties of plasmonic black absorbers and revised the manuscript.

Data Availability Statement

All data that support the findings of this study are available from the corresponding author upon reasonable request.

Keywords

black absorber, gas aggregation source, magnetron sputtering, plasmonic particles, RF sputtering

Received: July 3, 2023
Revised: August 23, 2023
Published online:

- [1] D. Abbott, presented at Proc. IEEE, 98, 42–66, Jan. 2010.
- [2] H. L. Zhang, J. Baeyens, J. Degrève, G. Cacères, *Renewable Sustainable Energy Rev.* **2013**, 22, 466.
- [3] E.-T. Hu, in *Optical Properties of Solar Absorber Materials and Structures*, (Eds: L.-Y. Chen), 142, Singapore: Springer, Singapore **2021**, pp. 1–165.
- [4] C. K. Ho, A. R. Mahoney, A. Ambrosini, M. Bencomo, A. Hall, T. N. Lambert, presented at ASME 2012 6th International Conference on Energy Sustainability, Parts A and B, American Society of Mechanical Engineers, San Diego, California, USA **2012**, pp. 509–518.
- [5] A. Dan, H. C. Barshilia, K. Chattopadhyay, B. Basu, *Renewable Sustainable Energy Rev.* **2017**, 79, 1050.
- [6] F. Gonzalez, E. Barrera-Calva, L. Huerta, R. S. Mane, *Open Surf. Sci. J.* **2011**, 3, 131.
- [7] E. Randich, D. D. Allred, *Thin Solid Films* **1981**, 83, 393.
- [8] J. Moon, D. Lu, B. VanSanders, T. K. Kim, S. D. Kong, S. Jin, R. Chen, *Nano Energy* **2014**, 8, 238.
- [9] L. Yang, L. Mo, T. Chen, E. Forsberg, S. He, *J. Appl. Phys.* **2015**, 118, 183103.
- [10] K. Valletti, D. M. Krishna, S. V. Joshi, *Sol. Energy Mater. Sol. Cells* **2014**, 121, 14.
- [11] L. Rebouta, P. Capela, M. Andritschky, *Sol. Energy Mater. Sol. Cells* **2012**, 105, 202.
- [12] N. P. Sergeant, M. Agrawal, P. Peumans, *Opt. Express* **2010**, 18, 5525.
- [13] J. Chen, H. Ye, L. Ae, Y. Tang, D. Kieven, T. Rissom, J. Neuendorf, M. C. Lux-Steiner, *Sol. Energy Mater. Sol. Cells* **2011**, 95, 1437.
- [14] H. C. Barshilia, N. Selvakumar, K. S. Rajam, A. Biswas, *J. Appl. Phys.* **2008**, 103, 023507.
- [15] H. C. Barshilia, N. Selvakumar, G. Vignesh, K. S. Rajam, A. Biswas, *Sol. Energy Mater. Sol. Cells* **2009**, 93, 315.
- [16] L. Zheng, F. Zhou, Z. Zhou, X. Song, G. Dong, M. Wang, X. Diao, *Sol. Energy* **2015**, 115, 341.
- [17] Y. Xue, C. Wang, W. Wang, Y. Liu, Y. Wu, Y. Ning, Y. Sun, *Sol. Energy* **2013**, 96, 113.
- [18] M. K. Hedayati, M. Javaherirahim, B. Mozooni, R. Abdelaziz, A. Tavassolizadeh, V. Sai Kiran Chakravadhanula, V. Zaporotchenko, T. Strunkus, F. Faupel, M. Elbahri, *Adv. Mater.* **2011**, 23, 5410.
- [19] N. Perdana, J. Drewes, F. Pohl, A. Vahl, T. Strunkus, M. Elbahri, C. Rockstuhl, F. Faupel, *Micro and Nano Engineer.* **2022**, 16, 100154.
- [20] M. A. Kats, D. Sharma, J. Lin, P. Genevet, *Appl. Phys. Lett.* **2012**, 101, 221101.
- [21] F. Garnich, E. Sailer, *Solar Energy Materials* **1990**, 20, 81.
- [22] X. Wang, H. He, J. Gao, H. Hu, S. Tang, X. Li, X. Li, H. Cao, *J. Mater. omics* **2021**, 7, 1103.
- [23] F. Cao, L. Tang, Y. Li, A. P. Litvinchuk, J. Bao, Z. Ren, *Sol. Energy Mater. Sol. Cells* **2017**, 160, 12.
- [24] H. C. Barshilia, P. Kumar, K. S. Rajam, A. Biswas, *Sol. Energy Mater. Sol. Cells* **2011**, 95, 1707.
- [25] Z. Wu, J. Wang, Y. Liu, S. Hou, X. Liu, Q. Zhang, F. Cao, *Materials Today Physics* **2021**, 18, 100388.
- [26] Y. Wu, E.-T. Hu, Q.-Y. Cai, J. Wang, Z.-Y. Wang, H.-T. Tu, K.-H. Yu, L.-Y. Chen, W. Wei, *Appl. Surf. Sci.* **2021**, 541, 148678.
- [27] K.-H. Su, Q.-H. Wei, X. Zhang, J. J. Mock, D. R. Smith, S. Schultz, *Nano Lett.* **2003**, 3, 1087.
- [28] D. W. Reicher, R. Christian, P. Davidson, S. Z. Peplinski, in *the SPIE Solar Energy + Technology*, (Eds: A. E. Delahoy, L. A. Eldada), San Diego, CA, **2009**, 740909.
- [29] G. Bräuer, *Surf. Coat. Technol.* **1999**, 112, 358.
- [30] F. Cao, K. McEnaney, G. Chen, Z. Ren, *Energy Environ. Sci.* **2014**, 7, 1615.
- [31] V. Baranau, U. Tallarek, *Soft Matter* **2014**, 10, 3826.
- [32] I. Fernandez-Corbaton, D. Beutel, C. Rockstuhl, A. Pausch, W. Klopper, *ChemPhysChem* **2020**, 21, 878.
- [33] M. I. Mishchenko, L. D. Travis, A. A. Lacis, *Lacis, Scattering, absorption, and emission of light by small particles*. Cambridge, Cambridge University Press, New York **2002**.
- [34] B. Zerulla, R. Venkitakrishnan, D. Beutel, M. Krstić, C. Holzer, C. Rockstuhl, I. Fernandez-Corbaton, *Adv. Opt. Mater.* **2023**, 11, 2201564.
- [35] D. Beutel, A. Groner, C. Rockstuhl, I. Fernandez-Corbaton, *J. Opt. Soc. Am. B* **2021**, 38, 1782.
- [36] C. Menzel, C. Rockstuhl, T. Paul, F. Lederer, T. Pertsch, *Phys. Rev. B* **2008**, 77, 195328.
- [37] T. G. Mackay, A. Lakhtakia, in *Synthesis Lectures on Electromagnetics*, Cham: Springer International Publishing, Switzerland **2020**.